across the fuse and β is a free parameter corresponding to the temperature. P. Perona and J. Malik [in *Proceedings of the IEEE International Symposium on Circuits and Systems* (Espoo, Finland, 1988) (IEEE, New York, 1988), pp. 2565–2568] have simulated similar elements using anisotropic diffusion.
12. For a two-terminal, voltage-controlled resistor characterized by $I = f(V)$, the co-content is defined as $J(V) = \int_0^V f(V')dV'$. For a linear resistor $I = GV$ and $J = GV^2/2$, half of the dissipated power $P = GV^2$. For stability results, see J. G. Harris, C. Koch, J. Luo, and J. Wyatt [in *Analog VLSI Implementations of Neural Systems*, C. Mead and M. Ismail, Eds. (Kluwer, Norwell, MA, 1989), pp. 27–56].
13. See C. Mead, *Analog VLSI and Neural Systems* (Addison-Wesley, Reading, MA, 1989). Our chip contains about 40,000 transistors, uses a 2.0-μm *n*-well complementary metal oxide semiconductor process, and was fabricated via MOSIS, the government-sponsored silicon foundry. Gate voltages are typically around 1.0 V.
14. J. M. Ortega and W. C. Rheinboldt, *Iterative Solution of Nonlinear Equations in Several Variables* (Academic Press, New York, 1970).
15. J. M. Hutchinson and C. Koch, in *Neural Networks for Computing*, J. Denker, Ed. (American Institute of Physics, New York, 1986), pp. 235–240; W. C. Elmore, *J. Appl. Phys.* **19**, 55 (1948).
16. J. G. Harris, C. Koch, E. Staats, J. Luo, *Int. J. Comput. Vision*, in press.
17. C. Koch, J. Harris, J. Luo, A. Hsu, T. Horiuchi, in *Neural Information Processing Systems 2*, D. Touretzky, Ed. (Morgan Kaufmann, Palo Alto, CA, in press).
18. Our analog circuitry consumes < 0.1 mW of power.
19. For a review of analog circuits for vision, see C. Koch, *Neural Comput.* **1**, 184 (1989); B. K. P. Horn, *Artif. Intell. Lab. Memo No. 1071* (1989).
20. We thank C. Mead for support. All chips were fabricated through MOSIS with the support of the Defense Advanced Research Projects Agency. Our research is supported by NSF grant IST-8700064, an NSF Presidential Young Investigator Award (to C.K.), a grant from the Office of Naval Research, DDF-II funds from the Jet Propulsion Laboratory at the California Institute of Technology, and funds from the Rockwell International Science Center and the Hughes Aircraft Artificial Intelligence Center. J.G.H. is a Hughes Aircraft Corporation fellow.

28 December 1989; accepted 12 April 1990

Structural and Electronic Role of Lead in $(PbBi)_2Sr_2CaCu_2O_8$ Superconductors by STM

XIAN LIANG WU, ZHE ZHANG, YUE LI WANG, CHARLES M. LIEBER*

The structural and electronic effects of lead substitution in the high-temperature superconducting materials $Pb_xBi_{2-x}Sr_2CaCu_2O_8$ have been characterized by scanning tunneling microscopy (STM) and scanning tunneling spectroscopy (STS). Large-area STM images of the Bi(Pb)–O layers show that lead substitution distorts and disorders the one-dimensional superlattice found in these materials. Atomic-resolution images indicate that extra oxygen atoms are present in the Bi(Pb)–O layers. STS data show that the electronic structure of the Bi(Pb)–O layers is insensitive to lead substitution within ±0.5 electron volt of the Fermi level; however, a systematic decrease in the density of states is observed at ≈1 electron volt above the Fermi level. Because the superconducting transition temperatures are independent of x(Pb) ($x \leq 0.7$), these microscopic STM and STS data suggest that the lead-induced electronic and structural changes in the Bi(Pb)–O layer do not perturb the electronic states critical to forming the superconducting state in this system.

SUBSTITUTION OF METALS IN THE RECENTLY discovered high-temperature superconductors has been used extensively both to probe factors that determine superconductivity and to prepare new materials (*1*). A case in point is Pb substitution in the Bi–O layers of Bi-Sr-Ca-Cu oxide materials (Fig. 1). Since Sunshine and co-workers first reported that the substitution of Pb enhances the superconducting onset temperature from 85 to 107 K in multiphase ceramic samples (*2*), numerous investigations of this chemical modification have been reported (*3–13*). In polycrystalline $(PbBi)_2Sr_2Ca_{n-1}Cu_nO_{2n+4}$ materials, Pb substitution has been found to favor the formation of the 110 K, $n = 3$ (2223) phase versus the 85 K, $n = 2$ (2212) phase (*8, 9*). In addition, diffraction studies have shown that the prominent one-dimensional incommensurate superstructure observed in $Bi_2Sr_2CaCu_2O_8$ changes upon substitution of Pb, although the details of these changes appear to be sample-dependent (*3–7*). Hence, it is not yet known how Pb substitution affects the intrinsic superconducting properties of these materials.

To probe directly the structural and electronic effects of Pb substitution, we studied high-quality, single-crystal $Pb_xBi_{2-x}Sr_2CaCu_2O_8$ ($x = 0$, 0.3, or 0.7) materials by scanning tunneling microscopy (STM) and scanning tunneling spectroscopy (STS). STM and STS are ideal techniques for characterizing the structural and electronic effects of Pb substitution because Pb primarily replaces Bi in the Bi–O layers (*10, 11*) and the $Pb_xBi_{2-x}Sr_2CaCu_2O_8$ crystals can be cleaved to expose a Bi(Pb)–O layer at the surface (Fig. 1).

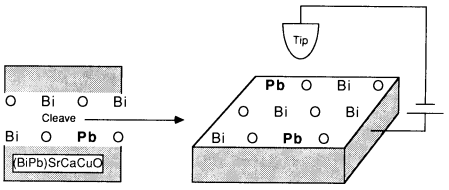

Fig. 1. Schematic view of $Pb_xBi_{2-x}Sr_2CaCu_2O_8$ showing the Bi(Pb)–O double layer and the surface STM geometry in these experiments. The bulk structure consists of a repeating sequence of Bi(Pb)–O, Sr–O, Cu–O, Ca, Cu–O, Sr–O, and Bi(Pb)–O layers as described by Sunshine *et al.* (*2*).

Single-crystal samples with the nominal composition $Pb_xBi_{2-x}Sr_2CaCu_2O_8$ ($x = 0$, 0.3, or 0.7) were grown from melts rich in CuO. Briefly, a homogeneous mixture of PbO, Bi_2O_3, $SrCO_3$, $CaCO_3$, and CuO powders was heated at 980°C for 10 hours, cooled at 2°C per hour to 800°C, and then furnace-cooled to room temperature. Bulk and surface analyses demonstrated that Pb was incorporated into these crystals at close to the Pb/Bi stoichiometry of the melts, although the Sr and Ca concentrations were slightly deficient with respect to the ideal 2212 formula. Single-crystal x-ray diffraction studies further showed that the crystal structures of the x(Pb) = 0 to 0.7 materials are the same (*14*); these data are in agreement with the results of earlier reports (*4, 8, 9*). The values of the superconducting transition temperature T_c (zero resistance) determined from dc resistivity measurements on at least five crystals are (T_c ± 1 SD) 85 ± 4, 88 ± 3, and 85 ± 2 K for the x = 0, 0.3, and 0.7 compositions, respectively. The sharp transitions observed for our materials [ΔT(90 to 10%) = 3 to 4 K] are indicative of high-quality materials. Furthermore, magnetic measurements (Meissner effect) demonstrate that the x(Pb) = 0, 0.3, and 0.7 crystals have similar bulk superconducting fractions. These structural, electrical, and magnetic data indicate that our crystals have reproducible macroscopic properties and hence are ideal for high-resolution STM studies.

All of the STM and STS studies of the $Pb_xBi_{2-x}Sr_2CaCu_2O_8$ materials were performed in an Ar-filled glove box equipped with a purification system that reduced the concentrations of H_2O and O_2 to below 1 ppm. The glove box environment, $PO_2 \approx 10^{-3}$ torr, was used to reduce the possibility of O_2 loss from the surface of the materials that may occur in ultrahigh vacuum (*12, 15*), at $PO_2 = 10^{-10}$ to 10^{-11} torr. The modified tunneling microscopes used in

Department of Chemistry, Columbia University, New York, NY 10027.

*To whom correspondence should be addressed.

this study (Nanoscope, Digital Instruments, Inc., Santa Barbara, California) have been described (*13, 16*). Reproducible images and spectroscopic measurements were obtained from in situ cleaved samples; the Bi(Pb)–O layers produced by cleaving (Fig. 1) were stable for at least 3 hours. Images were acquired in the constant current mode on at least six independent crystals for each Pb concentration with sample versus tip bias voltages (absolute values) between |150 and 450 mV| and tunneling currents between 0.3 and 1.5 nA. The tips used in all of the experiments were a Pt-Ir alloy (80% Pt, 20% Ir). For these conditions the images were stable and reproducible from sample to sample at a fixed Pb concentration. We made STS measurements by averaging 20 to 40 tunneling current versus bias voltage (*I-V*) curves at selected surface sites.

A series of 450 by 450 Å^2 gray-scale images of the Bi(Pb)–O layer recorded from x(Pb) = 0, 0.3, and 0.7 crystals are shown in Fig. 2. Images of the x(Pb) = 0 and 0.3 samples exhibit a one-dimensional superstructure, whereas images of the x(Pb) = 0.7 samples do not show a regular superstructure. The average period of the superstructure for the x(Pb) = 0 material determined from the analysis of 44 images was 24.6 Å; in terms of the tetragonal cell axes (Fig. 2) the incommensurate superstructure period was 4.6 *a* ($a \approx 5.4$ Å). This average period is in agreement with the results of recent diffraction (*5, 6, 17, 18*) and ultrahigh vacuum (UHV) STM (*19, 20*) studies. Although several models have been proposed to explain this one-dimensional superstructure (*5, 6, 19, 21*), it appears that the model most consistent with experimental data involves the insertion of an extra O into the Bi–O layer every nine to ten Bi sites (*6, 21*); the extra O causes the Bi–O layer to expand and buckle. This model suggests that the superstructure period should vary in real space. Careful analysis of the STM images for x(Pb) = 0 samples demonstrates that the superstructure period is not a regular sinusoidal modulation. The period varies (±1 SD) from 22.5 to 26.7 Å, and the distribution of periods about the average is broad and non-Gaussian. It is unlikely that these results are due to an analysis error because measurements of the charge density wave period in $TaSe_2$ (which has a known sinusoidal superstructure) yield a tight Gaussian distribution about the average wavelength.

The average period of the superstructure in the x(Pb) = 0.3 samples, 32.1 Å, is significantly larger than that observed in the unsubstituted samples and is consistent with diffraction studies of similar materials (*3–7*). On the basis of formal valence considerations (that is, Pb^{2+} versus Bi^{3+}), an increase in the period is expected because fewer extra O atoms will be incorporated into the Bi(Pb)–O layers. Our real-space STM images of x(Pb) = 0.3 samples also show several new features. In general, the superstructure is less regular than in the x(Pb) = 0 materials as evidenced by the random wavelike displacements along *a*. The distorted superstructure period varies (±1 SD) from 25.1 to 39.1 Å, which is a 10 Å greater variation than observed for the x(Pb) = 0 samples. In addition, two individual superstructure modulations will often distort sufficiently along *a* so as to merge (Fig. 2B). The distortions of the superlattice are most likely due to the random substitution of Pb for Bi in the Bi(Pb)–O planes and the associated differences in Pb–O versus Bi–O bonding. Significantly, the superlattice distortions imaged directly by STM account for the origin of the decrease in the superlattice "correlation length" determined by diffraction (*3*).

Convincing support for our suggestion that random Pb substitution distorts the superlattice is found in images of the x(Pb) = 0.7 materials (Fig. 2C). The super-

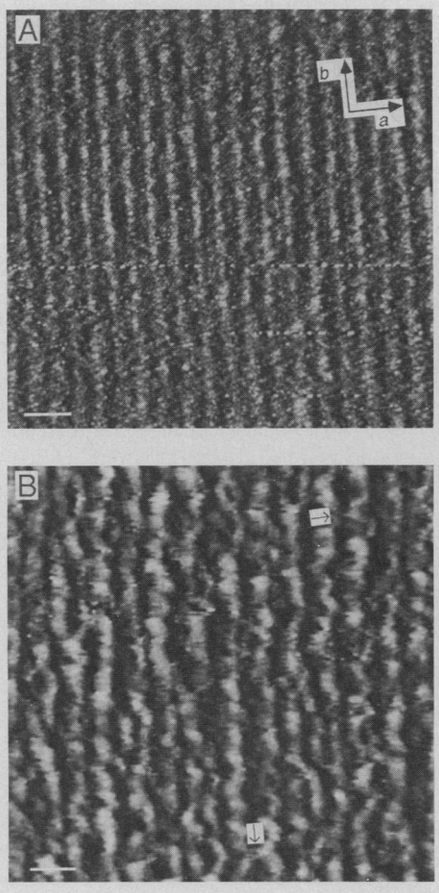

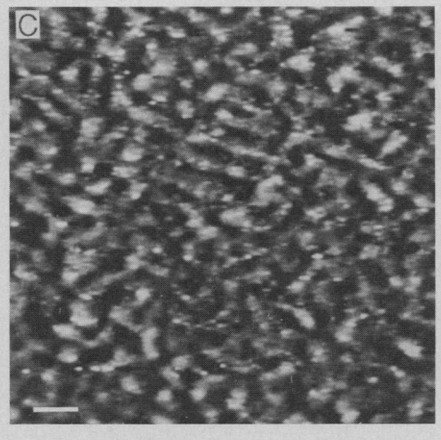

Fig. 2. Unfiltered STM images of (**A**) $Bi_2Sr_2CaCu_2O_8$, (**B**) $Pb_{0.3}Bi_{1.7}Sr_2CaCu_2O_8$, and (**C**) $Pb_{0.7}Bi_{1.3}Sr_2CaCu_2O_8$ samples recorded with ratios of bias voltage to tunneling current of 250 mV to 0.6 nA, 330 mV to 0.3 nA, and 400 mV to 0.8 nA, respectively. Several large distortions along *a* that result in the merger of two superstructure modulations are marked in (B). The white bar corresponds to 50 Å.

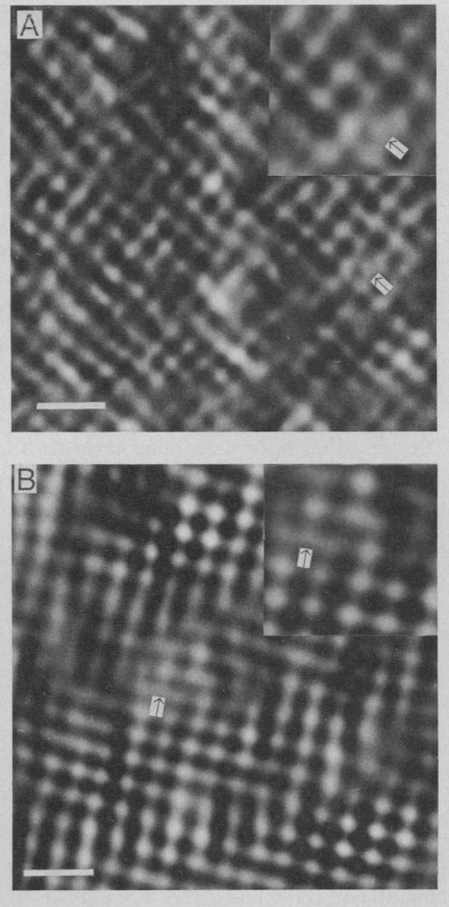

Fig. 3. Atomic-resolution images of x(Pb) = 0 (**A**) and x(Pb) = 0.3 (**B**) samples recorded with ratios of bias voltage to tunneling current of 250 mV to 0.6 nA and 450 mV to 0.3 nA, respectively. The images have been filtered with a spatial cutoff of 1.9 Å. The tetragonal surface structure is distorted in several areas. Extra atomic sites (marked with arrows) in the 15 by 15 Å^2 insets in (A) and (B) indicate that the distortions can be caused by the insertion of an additional atom into the lattice. The white bar represents 10 Å.

structure in these images is not periodic at all but rather exhibits near-random disorder as expected for the high level of Pb in the Bi(Pb)–O layers. This highly disordered superstructure is also observed in images of x(Pb) = 0.7 crystals grown at slower and faster cooling rates (1° to 10°C per hour) and crystals grown from melts rich in Bi_2O_3 and PbO rather than CuO. We believe therefore that this disorder is representative of the intrinsic structure of the heavily substituted materials.

We have also recorded atomic-resolution images of the x(Pb) = 0 to 0.7 materials to probe the origin of the Pb-induced variations in the superstructure (Fig. 3). High-resolution images of these materials recorded with bias voltages |150 to 450 mV| are surprisingly similar. The average lattice periods for the x(Pb) = 0, 0.3, and 0.7 samples (3.7 ± 0.1, 3.8 ± 0.3, 3.7 ± 0.2, respectively) are the same within experimental error, although individual atomic distances may vary significantly (see below). These atomic distances are consistent with both the average O–O and the average Bi–Bi distances determined by crystallography (*2*). However, we attribute the structure to an image of the O sites in the Bi(Pb)–O layer because (i) inverse photoemission studies of the unsubstituted material indicate that the electronic states near the Fermi level (that is, the states that are imaged in our low-bias STM measurements) are predominantly O 2p-π states (*22*), and (ii) it is likely that the electronic differences between Pb and Bi would be detected if we were imaging the states associated with these sites. Although our data cannot be used to map out the metal sites in the lattice, they do provide strong support for the proposal (*6, 21, 23*) that extra O is inserted into the Bi(Pb)–O layers. The insets in Fig. 3 highlight two areas where the tetragonal lattice structure is distorted by the addition of an extra atomic site (*24*). Notably, the site-site separation in the distorted regions, ≈2.4 Å, is close to the predicted O–O separation (*6, 21, 23*). These distorted regions are observed reproducibly in high-quality atomic-resolution images, although at present the images are too small to permit quantification of the number of extra atoms per superlattice modulation. The failure to observe this structure in earlier UHV STM studies (*19, 20*) may be due to the loss of O from the surface in vacuum (*12, 17*).

Lastly, we have been able to characterize systematic changes in the electronic structure of the Bi(Pb)–O layer as a function of x(Pb) by STS. Typical plots of the normalized conductivity, $(V/I)dI/dV$, versus sample-tip bias voltage are shown in Fig. 4. The data for the x(Pb) = 0 material are similar

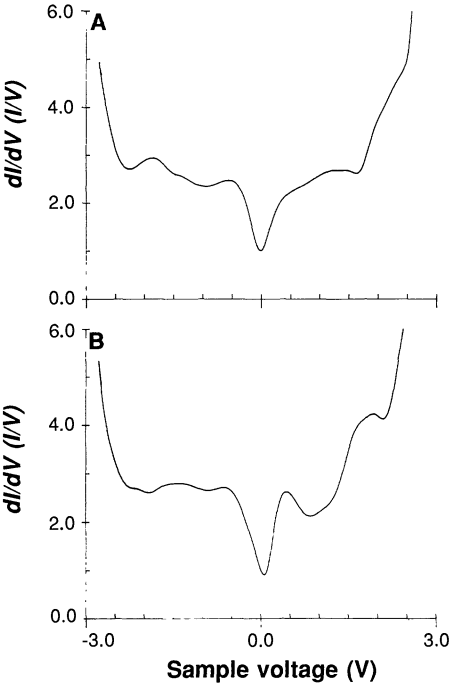

Fig. 4. Plots of the normalized conductivity versus sample voltage for x(Pb) = 0 (**A**) and x(Pb) = 0.7 (**B**) materials. The voltage corresponds to the energy relative to the Fermi level (V = 0).

to those reported in earlier UHV STM studies (*20*). As discussed elsewhere (*25*), $(V/I)dI/dV$ is proportional to the local density of states (DOS) at the sample surface, and thus these curves provide a direct record of the electronic structure of the Bi(Pb)–O layer. Between −0.6 and 0.4 eV the x(Pb) = 0 to 0.7 materials exhibit a partial gap in the DOS, which suggests that the Bi(Pb)–O layers are weakly metallic (*13*). The similarity of the DOS in this regime is consistent with the similar atomic structure observed in images recorded between |0.15 and 0.45 V| and with the suggestion (*20, 22*) that O 2p states dominate the electronic structure near the Fermi level. There is, however, a pronounced decrease in the density of empty electronic states at +1 eV for the x(Pb) = 0.7 versus x(Pb) = 0 samples (*26*). Recent inverse photoemission experiments (*22*) and theoretical calculations (*27*) indicate that this decrease in the unfilled states may be due to a decrease in the density of Bi 6p states as Bi is replaced by Pb or to changes in the O 2p DOS (a result of differences in the O–Pb versus O–Bi interaction). These spectroscopic differences are reproducibly observed with different samples in our experiments. In contrast, the STS data obtained between 0 and −2.5 V indicate that the filled states are not affected significantly by Pb substitution.

These spectroscopic results have several important implications. First, the clear differences in the empty states at ≈1 eV as x(Pb) increases indicate that it may be possible to determine the location of the Pb versus Bi sites in the lattice by acquiring images simultaneously at a low bias voltage and near 1 V. Second and perhaps most important, because T_c is independent of x(Pb) ($x \leq 0.7$), it is apparent that the changes in the Bi(Pb)–O layer DOS near 1 eV are sufficiently removed from the Fermi level that they do not interact with the electronic states critical in determining superconductivity in this system. Hence, it is interesting to speculate whether or not the Bi(Pb)–O layers are necessary other than as a structural building block. Substitution of metals (M) that perturb the electronic states of the Bi(M)–O layer closer to the Fermi level should test this idea.

REFERENCES AND NOTES

1. A. W. Sleight, *Science* **242**, 1519 (1988); R. J. Cava *et al.*, *Nature* **336**, 211 (1988).
2. S. A. Sunshine *et al.*, *Phys. Rev. B* **38**, 893 (1988).
3. C. H. Chen, D. J. Werder, G. P. Espinosa, A. S. Cooper, *ibid.* **39**, 4686 (1989); D. J. Werder, C. H. Chen, S. Jin, R. C. Sherwood, *J. Mater. Res.* **4**, 748 (1989).
4. J. Schneck, L. Pierre, J. C. Toledano, C. Daguet, *Phys. Rev. B* **39**, 9624 (1989).
5. P. Bordet *et al.*, *Studies High Temp. Supercond.* **2**, 171 (1989).
6. H. W. Zandbergen, W. A. Groen, F. C. Mijlhoff, G. van Tendeloo, S. Amelinckx, *Physica C* **156**, 325 (1988).
7. R. Ramesh, G. van Tendeloo, G. Thomas, S. M. Green, H. L. Luo, *Appl. Phys. Lett.* **53**, 2220 (1988); K. K. Fung, C. Y. Yang, Y. F. Yan, *ibid.* **55**, 280 (1989).
8. R. Ramesh *et al.*, *Phys. Rev. B* **38**, 7070 (1988).
9. H. K. Liu *et al.*, *Physica C* **157**, 93 (1989).
10. R. Ramesh *et al.*, *J. Appl. Phys.* **66**, 4878 (1989).
11. H. Nobumasa *et al.*, *Jpn. J. Appl. Phys.* **28**, L57 (1989).
12. N. Miura *et al.*, *ibid.*, p. L1112.
13. Z. Zhang, Y. L. Wang, X. L. Wu, J.-L. Huang, C. M. Lieber, in preparation.
14. Y. L. Wang and C. M. Lieber, unpublished results.
15. J. E. Demuth, B. N. J. Persson, F. Holtzberg, G. V. Chandrashekhar, *Phys. Rev. Lett.* **64**, 603 (1990).
16. X. L. Wu and C. M. Lieber, *Science* **243**, 1703 (1989); S. P. Kelty and C. M. Lieber, *Phys. Rev. B* **40**, 5856 (1989).
17. Y. Gao, P. Lee, P. Coppens, M. A. Subramanian, A. W. Sleight, *Science* **241**, 954 (1988).
18. T. M. Shaw *et al.*, *Phys. Rev. B* **37**, 9856 (1988).
19. M. D. Kirk *et al.*, *Science* **242**, 1673 (1988).
20. C. K. Shih, R. M. Feenstra, J. R. Kirtley, G. V. Chandrashekhar, *Phys. Rev. B* **40**, 2682 (1989); M. Tanaka *et al.*, *Nature* **339**, 691 (1989).
21. Y. Le Page, W. R. McKinnon, J.-M. Tarascon, P. Barboux, *Phys. Rev. B* **40**, 6810 (1989).
22. W. Drube, F. J. Himpsel, G. V. Chandrashekhar, M. W. Shafer, *ibid.* **39**, 7328 (1989); R. Claessen *et al.*, *ibid.*, p. 7316.
23. C. C. Torardi, J. B. Parise, M. A. Subramanian, J. Gopalakrishnan, A. W. Sleight, *Physica C* **157**, 115 (1989).
24. It is unlikely that this addition is due to a multiple tip effect because the lattice in adjacent parts of the image is tetragonal.
25. R. M. Feenstra, J. A. Stroscio, A. P. Fein, *Surf. Sci.* **181**, 295 (1987).
26. A Pb atom adsorbed on the tip could also cause this change in the spectroscopic data. We believe that this explanation is unlikely because data recorded for x(Pb) = 0.3 samples (*13*) show a change at +1 eV that is intermediate between that for the x(Pb) = 0 and that for the x(Pb) = 0.7 samples; that is, if a Pb

atom were responsible for the change, then the data for x(Pb) = 0.3 and 0.7 samples should be the same.
27. J. Ren *et al.*, *Physica C* **158**, 501 (1989); L. F. Mattheiss and D. R. Hamann, *Phys. Rev. B* **38**, 5012 (1988).
28. We acknowledge helpful discussions with D. S. Ginley, E. L. Venturini, B. Morosin, and R. J. Baughman, and we thank Y. J. Uemura, G. M. Luke, and B. J. Sternlieb for assistance with the magnetic measurements. This work was supported by the David and Lucile Packard Foundation, the National Science Foundation, and Rohm and Haas.

17 January 1990; accepted 27 March 1990

Explosive Deep Water Basalt in the Sumisu Backarc Rift

J. GILL, P. TORSSANDER, H. LAPIERRE, R. TAYLOR, K. KAIHO, M. KOYAMA, M. KUSAKABE, J. AITCHISON, S. CISOWSKI, K. DADEY, K. FUJIOKA, A. KLAUS, M. LOVELL, K. MARSAGLIA, P. PEZARD, B. TAYLOR, K. TAZAKI

Eruption of 1-million-year-old tholeiitic basalt >1800 meters below sea level (>18 megapascals) in a backarc rift behind the Bonin arc produced a scoriaceous breccia similar in some respects to that formed during subaerial eruptions. Explosion of the magma is thought to have produced frothy agglutinate which welded either on the sea floor or in a submarine eruption column. The resulting 135-meter-thick pyroclastic deposit has paleomagnetic inclinations that are random at a scale of <2.5 meters. High magmatic water content, which is about 1.3 percent by weight after vesiculation, contributed to the explosivity.

DEEP WATER EXPLOSIVE VOLCANism is an unwitnessed phenomenon that frequently is appealed to as an explanation of marine volcaniclastic rocks (*1*). Unlike subaerial volcanoes, submarine ones vent to pressure greater than atmospheric and erupt into a medium that has higher density, heat capacity, and conductivity than air. Consequently, higher magmatic gas contents are necessary for internally driven explosions, exsolved gas differs in composition, clasts quench faster, and eruption dynamics differ. This contrast also applies to volcanism into denser atmospheres on other planetary bodies such as Venus.

Before magma explodes it vesiculates. Tholeiitic basalt lavas with more than 10% vesicles by volume generally erupt in water shallower than 500 to 800 m below sea level (mbsl) and outgas mostly CO_2 (*2*). More highly vesicular tholeiite lavas associated with deep water sediments are most common in backarc basins (*3*). Submarine pyroclastic rocks are also common in the geologic record but most are sufficiently old that their geologic setting at the time of eruption is uncertain and their volcanologically diagnostic characteristics have degraded. There is disagreement whether the responsible explosions occurred in deep water (*1*) and were internally or externally driven. Explosivity due to exsolution of magmatic gas is thought to require gas/melt ratios of about 3 (*4*), whereas externally driven steam explosivity merely requires vigorous dynamic contact between magma and water (*5*). The maximum pressure for either kind of explosivity is unknown, but has been thought to be 10 to 30 MPa (*6*). In this report we describe a late Pleistocene scoriaceous tholeiitic basalt breccia that apparently erupted explosively at >1800 mbsl (18 MPa) during the initial rifting stage of a backarc basin. Eruption resulted in thorough fragmentation of the magma into frothy shards that then welded into agglutinate in the eruption column or on the sea floor. Consequently, all the traits described below that conventionally are associated with subaerial eruption—high vesicularity, explosivity, hot deposition, and thin cooling units—also can form at moderate pressure, for example, in deep water.

The breccia was discovered at Site 791 of

J. Gill, Earth Sciences Board and Institute of Marine Studies, University of California, Santa Cruz, CA 95060, USA.
P. Torssander, Department of Geology, University of Stockholm, S-106 91, Stockholm, Sweden.
H. Lapierre, Laboratoire de Geologie Structurale, Universite d'Orleans, 45067 Orleans Cedex 2 France.
R. Taylor, Department of Geology, University of Southampton, Hampshire S09 5NH England.
K. Kaiho, Institute of Geology and Paleontology, Tohoku University, Sendai 980 Japan.
M. Koyama, Institute of Geosciences, Shizuoka University, Shizuoka 422 Japan.
M. Kusakabe, Institute for Study of Earth's Interior, Okayama University, Misasa, Tottori-ken 682-02 Japan.
J. Aitchison, Department of Geology and Geophysics, University of New England, Armidale, NSW, Australia, 2351.
S. Cisowski, Department of Geological Sciences, University of California, Santa Barbara, CA 93106.
K. Dadey, Graduate School of Oceanography, University of Rhode Island, Kingston, RI 02811.
K. Fujioka, Ocean Research Institute, University of Tokyo, 1-15-1 Nakano, Tokyo 164 Japan.
A. Klaus and B. Taylor, Hawaii Institute of Geophysics, University of Hawaii, Honolulu, HI 96822.
M. Lovell, Geology Department, Leicester University, Leicester LE1, 7RH England.
K. Marsaglia, Department of Geology, University of Texas, El Paso, TX 79968.
P. Pezard, Lamont-Dohert Geological Observatory, Palisades, NY 10964.
K. Tazaki, Department of Geology, Shimane University, Matsue, Japan.

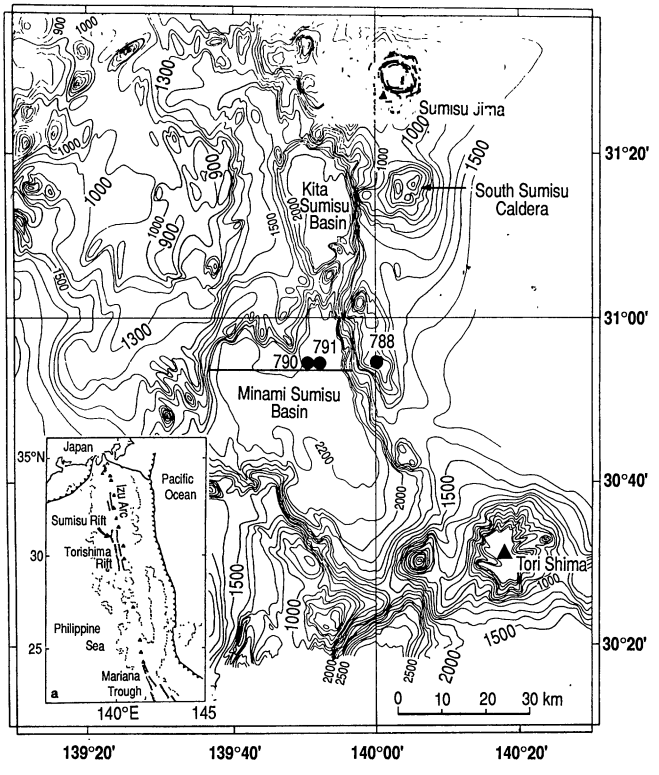

Fig. 1. Location map. Sites 788, 790, and 791 were drilled during ODP Leg 126. The volcanic arc extends from Sumisu Jima through Site 788 to Tori Shima. Kita and Minami Sumisu basins constitute the Sumisu Rift, the location of which is shown in the inset.